FUKUSHIMA DAIICHI UNIT 1 EX–VESSEL PREDICTION: CORE–CONCRETE INTERACTION

K. R. Robb*, M. W. Francis
Oak Ridge National Laboratory
P.O. Box 2008, Oak Ridge, TN 37830, USA
robbkr@ornl.gov, francismw@ornl.gov

M. T. Farmer
Argonne National Laboratory
9700 S. Cass Avenue, Argonne, IL 60439, USA
farmer@anl.gov

ABSTRACT

Lower head failure and corium–concrete interaction were predicted to occur at Fukushima Daiichi Unit 1 (1F1) by several different system-level code analyses, including MELCOR v2.1 and MAAP5. Although these codes capture a wide range of accident phenomena, they do not contain detailed models for ex-vessel core melt behavior. However, specialized codes exist for analysis of ex-vessel melt spreading (e.g., MELTSPREAD) and long-term debris coolability (e.g., CORQUENCH). On this basis, an analysis was carried out to further evaluate ex-vessel behavior for 1F1 using MELTSPREAD and CORQUENCH. Best-estimate melt pour conditions predicted by MELCOR v2.1 and MAAP5 were used as input. MELTSPREAD was then used to predict the spatially dependent melt conditions and extent of spreading during relocation from the vessel. The results of the MELTSPREAD analysis are reported in a companion paper. This information was used as input for the long-term debris coolability analysis with CORQUENCH.

KEYWORDS
Fukushima Daiichi, severe accident, ex-vessel, MCCI

1. INTRODUCTION

MELCOR simulations for Fukushima Daiichi Unit 1 (1F1), carried out as a part of a joint effort between the Department of Energy Office of Nuclear Energy (DOE-NE) and the Nuclear Regulatory Commission Fukushima Daiichi Accident Study [1], predicted major core melting, bottom head failure, and molten corium–concrete interaction (MCCI). These predictions are in agreement with simulations performed by the Electric Power Research Institute (EPRI) using the MAAP code [2], as well as the former Japanese Nuclear Energy Safety Organization using MELCOR [3] and the Tokyo Electric Power Company

(TEPCO) using MAAP [3,4]. Additionally, containment atmospheric monitoring system and reactor pressure vessel (RPV) temperature data, as well as energy balance analysis, suggested that melt has exited the RPV [5–7]. Both MELCOR and MAAP are capable systems-level modeling tools that capture a wide spectrum of accident phenomena in a tractable manner. However, for ex-vessel sequences, specialized codes containing more detailed modeling are available for the analysis of melt spreading (e.g., MELTSPREAD [8,9]), as well as debris coolability during MCCI (e.g., CORQUENCH [10,11]).

The objective of this work is to use CORQUENCH to provide more rigorous, best-estimate predictions and analysis of the long-term ex-vessel MCCI following postulated vessel failure at 1F1. The analysis is based on best-estimate melt pour conditions from MELCOR [1] and MAAP [2] simulations and best-estimate spreading results from MELTSPREAD [12, 13]. Other general goals of the study are to (1) provide results for comparison against MELCOR and/or MAAP results, (2) scope out the range of possible final debris configurations in containment, and (3) identify uncertainties in the predictions.

The approach used melt pour conditions following RPV failure obtained from the MELCOR [1] and MAAP [2] analyses as input to MELTSPREAD to generate predictions of melt spreading, basemat attack, cladding oxidation (viz. H_2/CO production), debris cooling, and drywell liner attack during the transient spreading phase. Since cavity conditions during the accident are uncertain, a sensitivity study was performed in MELTSPREAD to evaluate the effect of the presence/absence of water on the cavity floor, melt pour rate and temperature, and sump cover plate failure on the global spreading behavior. MELTSPREAD and CORQUENCH are two separate and distinct computer codes. Thus MELTSPREAD was used to define tabular input for CORQUENCH, which in turn evaluated the long-term debris cooling behavior [12, 13]. A parametric study was also conducted with CORQUENCH to evaluate the effects of various modeling options and boundary condition parameters.

A brief summary of CORQUENCH's modeling capabilities and validation status is provided first, followed by a description of the case scenarios and modeling assumptions used in the 1F1 analysis. The main results are then presented, followed by a summary of key findings from this study.

2. CORQUENCH DESCRIPTION

CORQUENCH [10] was originally developed to provide a simple, modular model of MCCI behavior that could readily be adapted to investigate the adequacy of melt/water heat transfer correlations as they were developed. It is capable of performing either a one-dimensional (1-D) or simplified 2-D ablation calculation (rectangular notch or cylindrical).

The MCCI conservation of energy equation includes the following energy source/sink terms: (1) decay heat; (2) mass flux of melt from the failed reactor pressure vessel; (3) chemical reactions between the metallic melt constituents Zr, Cr, Fe (in sequence) and concrete decomposition gases H_2O and CO_2; (4) condensed-phase chemical reactions between Zr and SiO_2; (5) downward (and sideward for the 2-D case) heat transfer to concrete; and (6) heat transfer to the overlying atmosphere (wet or dry). The melt composition can range from fully metallic to fully oxidic. The metallic and oxidic phases are assumed to be well mixed. The MCCI conservation of mass equations and thermophysical property subroutines consider most core and concrete metals and their corresponding oxides.

In terms of heat transfer at the melt/concrete interface, CORQUENCH incorporates a transient concrete ablation/decomposition model that accounts for the effects of transient concrete heat-up with simultaneous crust growth following initial melt contact with the concrete. The heat transfer coefficient at the melt/concrete interface can be selected from a variety of options, including (1) slag film model with bubble agitation, (2) gas film model, or (3) empirical correlations based on MCCI test results.

At the melt upper surface, radiant heat transfer to the overlying structure is calculated when the cavity is dry. When water is present, bulk cooling and incipient crust formation are calculated. Following incipient crust formation, crust growth is calculated by solving a growth rate equation; the crust material composition is treated separately from the melt material composition, which is important in long–term calculations in which significant mass may be frozen in the crust. For the case in which the crust is treated as permeable to water ingress, either the crust dry-out limit can be calculated using a user-specified crust permeability, or the dry-out heat flux can be calculated using the Lomperski-Farmer model [14]. Particle bed formation by the mechanism of melt eruptions is also evaluated. For situations in which water is present and a particle bed develops over the crust, the heat flux from the crust upper surface may be limited by the particle bed dry-out limit. One significant model shortcoming is that the code currently cannot correctly model situations in which the debris may dry out or be undercooled by virtue of inadequate water flooding supply. The scenario in which there is insufficient water addition to keep the debris covered with water is bounded by scenarios that assume either the debris is always covered by water or always dry.

The code includes a model to mechanistically calculate the occurrence of crust anchoring to test section sidewalls, as well as the subsequent melt/crust separation phase that arises as a result of concrete densification upon melting. This is an important experiment distortion, stemming from the size of the tests. The melt void fraction, which is relevant in determining the location where the crust anchors to the test section sidewalls in experiments, can be evaluated from one of several different correlations. Melt viscosity is calculated with a correction for SiO_2 and enhancement due to solids buildup within the melt.

CORQUENCH validation efforts have focused primarily on oxidic reactor material experiments. The approach for the code validation was to make a common set of user-specified modeling assumptions and apply those assumptions for all the analyzed tests. The validation matrix includes, wet and dry cavity tests 1-D and 2-D experiments, as well as tests conducted with siliceous, limestone–common sand, and limestone–limestone concrete. Descriptions of the validation matrix and results are provided in Ref. [10].

3. SUMMARY OF CASE SCENARIOS AND MODELING ASSUMPTIONS

3.1. Drywell Modeling Representation

To capture the spatial variation in melt depth and concrete ablation, the containment was divided into six regions: sumps (1), inner pedestal (2), inside edge of the pedestal (3), doorway (4) between the drywell and pedestal, an area extending from the doorway to the drywell liner (5), and the far-field drywell (6). These regions are numbered and illustrated in Figure 1. The containment has not previously been divided into computational regions for CORQUENCH simulations, and the methodology was developed as part of this work. Each region is modeled independently; i.e., there is no heat or mass transfer between regions as time progresses.

The 1F1 containment is a Mark I design. The regions were modeled in CORQUENCH using the three basic geometric modeling options available. The sumps (1) are modeled as 2-D cylindrical cavities with concrete walls that are higher than the melt. In reality, the sumps are square and the accumulated melt depth above the height of the sumps will not be in direct contact with the sump walls. However, based on the spreading results [13], most of the melt in the sumps would be in contact with the sump walls for all cases. The floor areas of the sumps (2.1025 m^2 each) were conserved so that the melt height was conserved. Only one sump was simulated, and the results were assumed to be the same for the other sump. The inner pedestal region (2) included 10.851 m^2 of area between and around the sumps. This region was modeled using the 1-D geometry option. The pedestal edge (3) region was modeled using a 2-D cylindrical geometry similar to that for the sumps. The diameter of the cavity was the same as that of the actual pedestal, 5.0 m. The amount of melt per unit of area in the edge region, as determined from the

MELTSPREAD results, was extrapolated to fill the inner portion of the 2-D cylinder. This conserved the melt height at the pedestal walls and the pedestal curvature. These parameters were conserved in order to conserve the heat and mass transfer at the walls. Other important parameters, such as combustible gas generation during core–concrete interaction, were scaled appropriately. The doorway region (4), the area outside the doorway (5), and the far-field drywell (6) were modeled as 2-D notch geometries. The doorway region (4) was modeled as a rectangular area (1.2 m^2) with two 1.2 m long concrete walls and two 1.0 m long adiabatic walls. The 90º spreading sector outside the pedestal door exit region (5) was modeled as a rectangular area (9.69 m^2) with two 3.4 m long concrete walls and two 2.85 m long adiabatic walls. The drywell (6) region included all of the drywell floor area except for the doorway exit region, which was covered in melt. The drywell was modeled as a rectangular area with two adiabatic walls 2.85 m in length (width between the pedestal and drywell liner). The floor area and concrete wall lengths were specified for each case to conserve the spread area predicted by MELTSPREAD.

Although the method used to discretize the containment for CORQUENCH simulations enables spatial variations of ablation to be evaluated, there are a few compromises and limitations associated with the technique. The heat transfer between regions is not captured. However, the cross-sectional area of melt in neighboring regions is much lower than that in contact with concrete and water (or the containment atmosphere), and the lateral heat transfer would be much lower than the heat transfer to the water (or atmosphere) and concrete. Mass transfer between regions, after the initial spreading, is also not modeled. The swelling of the melt by the gases released during concrete ablation may cause regions of the melt to rise and spread to other regions. Finally, radial ablation may cause regions to expand into one another. This effect will increase with the extent of radial ablation, but for most regions this influence is expected to be negligible.

In the 2-D notch geometry modeling option, CORQUENCH does not currently have the capability to independently specify each wall material. Therefore, the liner wall is modeled as concrete. Concrete ablation starts at 1500 K, which is lower than the melting point of the liner (~1810 K). In addition, CORQUENCH does not contain a detailed liner heat transfer model like that implemented in MELTSPREAD. Therefore, the ablation predictions by CORQUENCH, near the liner, are conservative. A more rigorous investigation of the melt-liner interface with the MELTSPREAD code is discussed in the companion paper [13].

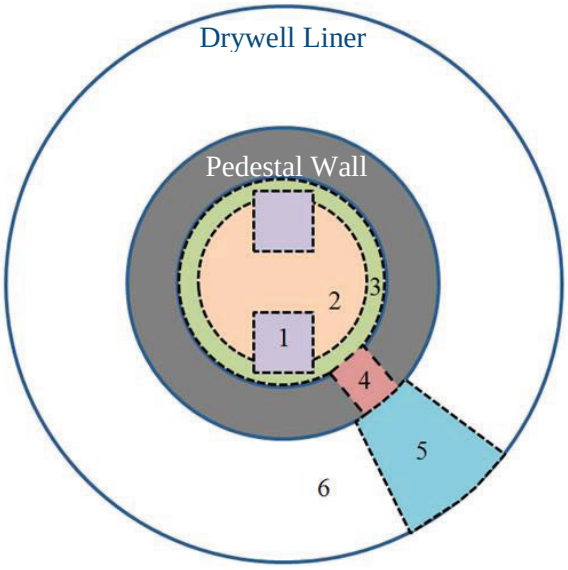

Figure 1. Discretization of Drywell.

3.2. Case Definition

3.2.1. Scenario input to CORQUENCH

The 1F1 plant response was previously evaluated independently with MELCOR v2.1 [1], by Sandia National Laboratories, and MAAP5 [2], through EPRI. These analyses were carried out up through the point of reactor vessel failure and discharge of the core melt into the reactor containment. Three pour scenarios from those analyses were used as input for MELTSPREAD analyses. These pour scenarios are summarized in Table I.

Table I. Melt pour scenarios

Case Designator	MELCOR	MAAP-LP	MAAP-HP
Sequence description	LP vessel failure	LP vessel failure	H vessel failure
Onset of pour (hours)	14.27	10.11	8.14
Pour duration (sec)	4030	17.5	5.3
Containment pressure (MPa)[b]	0.75	0.75	0.75
Water level on drywell floor (cm)	55	20	0
Melt pour temperature (K)	Range: 1850-2100 Average: 1975	2751	2797
Oxide phase solidus-liquidus (K)[a]	2215-2467	1934-2588	1925-2587
Metal phase solidus-liquidus (K)[a]	1705-1735	1802-1812	1803-1813
Melt solid fraction (-)[a]	0.56	0.0	0.0
Decay heat (W/kg fuel)	86	96	105
Pour mass of constituent (kg)			
UO_2	69400	76153.2	76153.4
Zr	25800	16594.1	16616.0
ZrO_2	16600	14141.5	14112.7
Cr	5900	1135.9	1099.4
Cr_2O_3	30	2732.0	2765.5
Fe	20430	16095.1	15928.4
FeO	230	11210.5	11369.5
Ni	2530	555.7	534.8
NiO	30	1208.2	1229.1
B_4C	0	502.0	502.0
Total	140950	140328.3	140310.8

[a]Calculated with CORQUENCH subroutines given composition and melt pour temperature
[b]Approximate; based on plant data [12].

One pour scenario was based on the pour predicted by MELCOR. It is a low-pressure sequence (with respect to RPV pressure) in which the vessel is predicted to fail at 14.27 h, leading to the gradual discharge of ~ 141 t of core debris into the drywell. The debris temperature just before the vessel failed ranged from 1850 to 2100 K. In this range of temperature, the melt is quite viscous because of the concentration of solids. The other two pour scenarios were based on low-pressure (MAAP-LP) and high-pressure (MAAP-HP) scenarios. In the MAAP-LP scenario, the vessel failed at 10.11 h, leading to rapid discharge of ~140 t of core debris into the pedestal. The water depth in the drywell for the MAAP-LP scenario was ~20 cm at vessel failure. The debris temperature at vessel failure was 2751 K; thus the melt was superheated by ~160 K relative to the oxide phase liquidus. In the MAAP-HP scenario, the vessel failed at 8.14 h. The pour mass and composition were similar to the LP scenario, except that the melt was more superheated (i.e., 210 vs. 160 K) and the pour duration was shorter.

MELTSPREAD was then used to evaluate the three melt pour scenarios (MELCOR, MAAP-LP, MAAP-HP). Several cases were evaluated for each sequence to examine the sensitivity of the spreading behavior to several factors. The cases are summarized in Table II. Cases 1–4 were simulated for all three pour scenarios. Cases 5–6 were simulated only for the MELCOR pour scenario. The MELTSPREAD simulations provide detailed melt locations, compositions, and temperature as well as the concrete ablation depths as functions of time and position, which are discussed in a companion paper [13].

For the MELCOR cases, MELTSPREAD predicted essentially no concrete ablation or additional cladding oxidation during the spreading phase. For the MAAP cases, MELTSPREAD predicted a modest amount of concrete ablation during the spreading phase (~2 m^3 in volume, principally located in the pedestal doorway and just outside the door). The MAAP-LP and -HP scenarios yielded similar amounts of ablation (i.e., average slag content in the melt was 2.5 and 2.8 wt % for the LP and HP scenarios, respectively). The three sets of melt composition (see Farmer et al. [13] and Table I), were used for all CORQUENCH simulations of the MELCOR, MAAP-HP, MAAP-LP scenarios. The relative fraction of oxide to metallic components in each of the six CORQUENCH computation regions (from the MELTSPREAD output) was conserved in the CORQUENCH simulations.

Table III summarizes the initial collapsed melt thicknesses and temperature in each of the discretized cavity regions for each of the best-estimate MELTSPREAD cases. For the MAAP cases, the melt thicknesses in the doorway and door exit regions were greater than in neighboring regions. The difference was due to concrete ablation occurring in the doorway and door exit regions during the spreading process.

Table II. MELTSPREAD scenarios

Case no.	Description/rationale	Parameter investigated
1	60 cm water level in drywell, sump plates fail at t=0	–
2	Case 1, but sump plates initially intact	Melt retention in sump
3	Case 1, but the cavity is dry	Dry cavity
4	Case 1, but cavity water level is limited to ½ vent line height (30 cm)	Water depth
5[a]	Case 1, but melt assumed to relocate in 10 seconds	Melt pour rate
6[a]	Case 2, but melt assumed to relocate in 10 seconds	Dry cavity and pour rate

[a] Modeled only for the MELCOR pour scenario

Table III. Initial melt depth and temperature in each region

	Initial collapsed melt thickness (cm) / Temperature (K) in each region					
Case	**Region 1**	**Region 2**	**Region 3**	**Region 4**	**Region 5**	**Region 6**
MELCOR-1[a]	187 / 2110	63 / 2110	46 / 2110	29 / 2110	21 / 2110	4 / 2110
MAAP-HP-3[a]	140 / 2763	16 / 2763	17 / 2523	29 / 2512	22 / 2485	13 / 2443
MAAP-LP-4[a]	139 / 2720	15 / 2720	16 / 2474	29 / 2485	20 / 2438	13 / 2366

[a] Case is considered the "best estimate" with respect to the melt pour and spreading analysis.

For the MELCOR cases, a large fraction of the melt was predicted to be solidified by the end of the MELTSPREAD simulation. CORQUENCH currently does not have the ability to model re-melting of solid debris when the debris is completely solid at the start of the simulation. Thus, to investigate the long-term coolability of the melt for this scenario, the initial melt temperature in CORQUENCH was artificially increased to 2110 K, a few degrees above the average core debris solidus temperature (2108 K)

for the oxide–metal mixture predicted by the CORQUENCH property subroutines [12]. CORQUENCH was then used to determine the long-term coolability of the melt with its advanced coolability and concrete ablation models. Thus, with this assumption, CORQUENCH evaluated the cooling behavior of a highly viscous melt interacting with concrete with an initial solid content of ~78%.

For the MAAP-HP and MAAP-LP cases, the temperature of the melt at the end of the spreading phase was still relatively high. The initial temperature in each of the CORQUENCH computational regions was specified based on the local temperatures predicted by MELTSPREAD at the end of the spreading phase (taken to be 120 s). These temperature distributions are summarized in Table III.

The composition of the concrete used in the construction of the Fukushima Daiichi plants is not known. Limited sampling has shown the concrete to have a high silicon and low calcium content [15], which is consistent with a siliceous type concrete. For use in comparison with other MELCOR analyses [1], the composition was chosen to be the same as the default basalt concrete composition, a form of siliceous concrete, which is embedded in MELCOR. For the duration of the simulations, the containment pressure (0.75 MPa), far field structural temperature (322 K), and emissivity (0.6) were held constant at the prescribed values. The dry-out of free water in the concrete was assumed to occur at the containment saturation temperature.

Two long-term containment conditions were investigated. In the first case, the cavity was assumed to remain dry until 15 h after SCRAM. At this point the cavity was then assumed to be flooded. As a bounding scenario, a case without water addition was also evaluated as part of the CORQUENCH parametric study. These two long–term containment conditions bounded the melt progression envelope.

In terms of CORQUENCH modeling options, all cases were executed using the concrete transient heat-up and decomposition (dry-out) model [10]. Any melt–concrete interstitial crusts were assumed to be porous, allowing slag to flow through the crusts into the melt. Based on validation calculations [10], the critical heat flux multipliers for determination of bulk cooling and film boiling breakdown were set at 0.5. The correlation by Farmer was used to model melt eruptions [16]. For cases in which particle beds formed, the bed porosity and average particle diameter were set to 40% and 2.8 mm, respectively; these values are based on post-test examination results reported as part of the MACE program [17]. Water ingression was calculated using the Lomperski–Farmer correlation developed as part of the OECD/MCCI program [14]. The empirical constant C in this model was set to 9.0 based on previous code validation work [10]. The crust anchoring modeling option was disabled. The impact of the crust anchoring phenomenon was investigated in the CORQUENCH parametric study (Section 4.2). The zirconium was assumed to be in solution with the core oxide phase, and condensed phase chemical reactions between Zr and SiO_2 were modeled. The top crust thermal conductivity was calculated using the code property subroutines. The effect of solids buildup in the melt was modeled with the Ishii-Zuber correlation with the maximum solids fraction set at 1.0. The effective melt freezing temperature was based on the solidus temperature for the metal and oxide phases. Melt void fraction was modeled using the correlation by Brockmann [10].

All cases were performed with a uniform time step of 0.05 s. The low time step was required for some cases to capture the transient growth of the thermal boundary layer in the concrete. The cases ended when either 2 days of real time simulation had passed, or the melt was completely solidified

The following nomenclature is used to indicate the case analyzed: Pour Scenario—MELTSPREAD Case—CORQUENCH Case. The “Pour Scenario” refers to either the MELCOR, MAAP-LP, or MAAP-HP pour scenario. The “MELTSPREAD Case” refers to the case number from Table II, and “CORQUENCH Case” refers to the case letter from Table IV. For example, MAAP-HP-3-A refers to the MAAP-HP melt pour scenario, the -3 MELTSPREAD case (dry cavity), and the -A CORQUENCH case (base case).

Table IV. CORQUENCH parametric study

Case	Description/rationale	Parametric effect investigated
A	CORQUENCH best-estimate models and conditions	None—base case
B	Case 1 except there is no water addition	Worse case—no water injection
C	Case 1 except the containment pressure is 0.35 MPa	Containment pressure
D	Case 1 except the melt-concrete crust formation is prohibited and uses quasi-steady concrete ablation model	Interstitial crusts and transient conduction on concrete ablation
E	Case 1 except the melt decay heat is 25% lower	Decay heat reduction due to the volatilization of radionuclides
F	Case 1 except crust anchoring to the cavity walls is allowed	Possible crust anchoring and separation from the melt pool
G	Case 2 except the melt-concrete crust formation is prohibited and uses quasi-steady concrete ablation model	Interstitial crusts and transient conduction on concrete ablation

4. RESULTS

For the three melt pour scenarios, a total of 14 MELTSPREAD simulations were conducted. For each of the 14 MELTSPREAD cases, 7 CORQUENCH parametric cases were simulated (Table IV). Each of these included separate simulations for the six regions in containment. Altogether, 588 CORQUENCH simulations were conducted [12]. Section 4.1 discusses the base case CORQUENCH results, while Section 4.2 summarizes the results of the parametric study.

4.1. Base Case Results

The melt was predicted to be coolable and quenched before the end of the simulation for the MELCOR-1-A, MAAP-HP-3-A, and MAAP-LP-4-A cases. Table V provides the time until melt solidification in the various regions (see Figure 1) for the three cases. Table VI provides the total axial and radial ablation in the various regions for the three cases.

Table V. Total CORQUENCH simulation time until melt solidification

	Simulation time until melt solidification (min)					
Case	**Region 1**	**Region 2**	**Region 3**	**Region 4**	**Region 5**	**Region 6**
MELCOR-1-A	151	63	42	24	18	2
MAAP-HP-3-A	1362	476	458	500	483	440
MAAP-LP-4-A	1176	349	333	376	352	319

Table VI. Total axial and radial concrete ablation

	Total axial/radial concrete ablation (cm)					
Case	**Region 1**	**Region 2**	**Region 3**	**Region 4**	**Region 5**	**Region 6**
MELCOR-1-A	13.4 / 19.9	8.9 / NA	6.9 / 2.2	5.1 / 0.7	4.4 / 0.2	1.3 / 0.0
MAAP-HP-3-A	64.1 / 64.1	23.4 / NA	16.2 / 16.3	21.5 / 21.7	22.5 / 22.6	11.4 / 11.5
MAAP-LP-4-A	58.8 / 58.8	21.1 / NA	14.4 / 14.6	20.2 / 20.2	19.1 / 19.2	10.1 / 10.3

In the MELCOR-1-A case, the melt quickly formed crusts at the melt–concrete interface. The interstitial crust acted to insulate the concrete from the melt and reduced or eliminated early concrete ablation. At the start of the CORQUENCH simulation, it was assumed water had already flooded the containment at 15 h after SCRAM. The melt was readily quenched by the overlying water. The sump region, where the melt pool was the deepest, underwent the most concrete ablation (13 cm axial, 20 cm radial) and took the longest (151 min) to solidify. The other regions (inner pedestal, pedestal edge, doorway, door exit, and drywell) experienced minor concrete ablation and the melt was readily cooled within 63 min of CORQUENCH simulation time.

The MAAP-HP-3-A case resulted in greater concrete ablation than the MELCOR-1-A case. All regions were predicted to be coolable and to eventually solidify. The high initial melt temperature (2443–2763 K) prohibited early crust formation at the melt–concrete interface. The sump region was predicted to experience approximately 64 cm of axial and radial concrete ablation before the melt solidified. This is less than the distance of the concrete between the sumps and the steel liner. The melt in the sumps took nearly 23 h to solidify after the onset of the melt pour. The melt in the regions other than the sump was predicted to solidify within 28–88 min after water addition at 15 h with moderate amounts of concrete ablation, 11.4–23.4 cm.

The MAAP-LP-4-A case results were very similar to those of the MAAP-HP-3-A case. However, the melt was released approximately 2 h later than in the MAAP-HP-3-A case. The reduced time between melt pour and water addition at 15 h resulted in slightly less concrete ablation than the MAAP-HP-3-A case. The high initial melt temperature (2366–2720 K) prohibited early crust formation at the melt–concrete interface. The sump region was predicted to experience approximately 59 cm of axial and radial concrete ablation before the melt solidified. The melt in the sumps took a little over 19.5 h to solidify after the onset of the melt pour. The melt in the regions other than the sump was predicted to solidify within 25–83 min after water addition at 15 h, with a moderate amount of concrete ablation, 10–21 cm.

The final cavity and debris profiles, along a vertical cross section of Figure 1, are illustrated in Figure 2 for the MELCOR-1-A and MAAP-HP-3-A cases. The final profile for the MAAP-HP-3-A and MAAP-LP-4- cases are quite similar.

For each region in each case, the axial and radial ablation depths are similar. This is due to the use of the same heat transfer and ablation model for the bottom and sidewalls. This is in contrast to experimental results using siliceous type concretes (i.e. MCCI-CCI-1 and CCI-3). In the MELCOR-1-A case, interstitial crusts formed at the concrete interface. Differences in the wall length scale, which influence

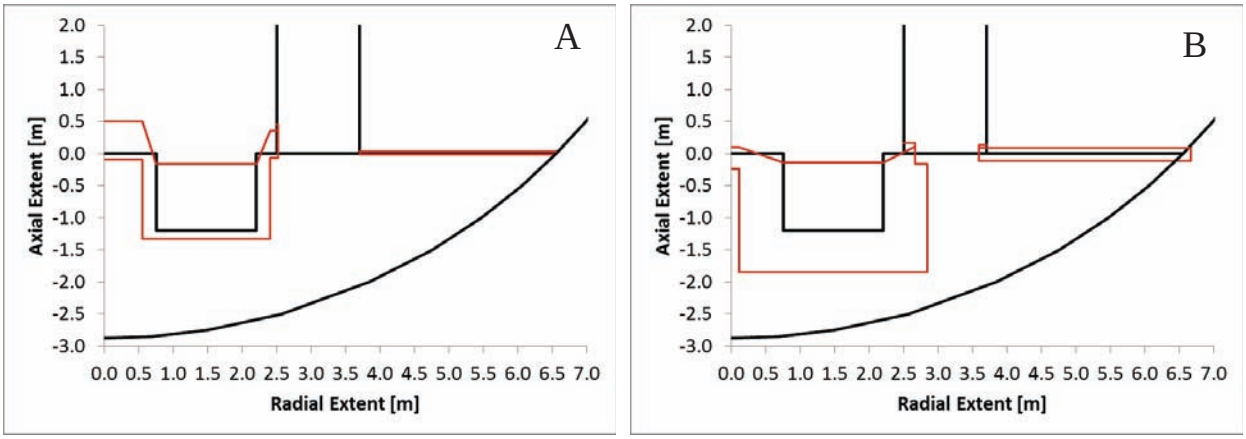

Figure 2. Final Cavity Profile for MELCOR-1-A (A) and MAAP-HP-3-A (B).

the predicted failure of the crusts, are the cause for the differences in the axial and radial ablation in each region for the MELCOR-1-A case. There is ongoing work to understand and model the causes for anisotropic ablation [18, 19].

The total amount of hydrogen, carbon monoxide, and carbon dioxide generated during the MCCI for the three cases is summarized in Table VII. Owing to the low temperatures, limited ablation, and relatively fast solidification, the MELCOR-1-A case resulted in limited gas generation. In contrast, both MAAP pour scenarios resulted in substantial amounts of gas generation.

Table VII. Total gas release

Case	H_2 (moles)	CO (moles)	CO_2 (moles)
MELCOR-1-A	37,400	3,690	10
MAAP-HP-3-A	348,000	26,900	11,200
MAAP-LP-4-A	345,000	26,300	7,310

Radial concrete ablation in the edge pedestal, doorway, door exit, and drywell regions can undercut the reactor pedestal. In addition to concrete ablation, CORQUENCH predicts the transient thermal boundary layer thickness in the concrete using a 1-D approximation and the assumption of a parabolic temperature profile [10]. This is of interest, as concrete loses compressive strength at elevated temperatures [20]. Based on the parabolic temperature profile assumption, the position, *x*, relative to the debris–concrete interface, of a temperature isotherm, *T(x)*, can be determined by Eq. (1), where T_{dc} is the concrete decomposition temperature (specified as 1500 K), T_i is the initial concrete temperature (specified as 322 K) and δ_{bl} is the boundary layer thickness.

$$x = \delta_{bl} \cdot \left(1 - \sqrt{\frac{T(x) - T_i}{T_{dc} - T_I}}\right) \tag{1}$$

Based on Eq. (1), approximately half the boundary layer thickness is above 615 K and a quarter of the boundary layer thickness is greater than 985 K. CORQUENCH does not include any models to predict the structural integrity of the pedestal. However, prediction of significant concrete ablation and a large heat-affected zone would suggest additional detailed modeling of the pedestal structural integrity may be warranted.

For the MELCOR-1-A case, the radial ablations of the edge pedestal and drywell regions were 2.2 and 0.0 cm, respectively. Compared with the pedestal wall thickness, 1.2 m, the predicted undercutting of the pedestal was very minor. The thermal boundary layer thickness in the pedestal wall at the end of the simulation was 5.9 cm on the interior wall of the pedestal and 1.6 cm on the outside wall of the pedestal. Thus the thermal-affected zone of the pedestal wall was also minor.

For the MAAP-HP-3-A case, the radial ablations of the edge pedestal and drywell regions were 16.3 and 11.5 cm, respectively. Thus 23% of the pedestal wall thickness at the base was predicted to be undercut by concrete ablation. The thermal boundary layer thicknesses in the pedestal wall at the end of the simulation were 39.9 cm on the interior wall of the pedestal and 38.1 cm on the outside wall of the pedestal. If half of the boundary layers were assumed to be a heat-affected zone, then a total of 66.8 cm at the base of the 1.2 m pedestal wall would be predicted to be either ablated away or in a heat-affected zone.

For the MAAP-LP-4-A case, the radial ablations of the edge pedestal and drywell regions were 14.6 and 10.3 cm, respectively. Thus 21% of the pedestal wall thickness at the base was predicted to be undercut by concrete ablation. The thermal boundary layer thicknesses in the pedestal wall at the end of the simulation were 36.2 cm on the interior wall of the pedestal and 33.8 cm on the outside wall of the pedestal. If half of the boundary layers were assumed to be a heat-affected zone, then a total of 59.9 cm at the base of the 1.2 m pedestal wall would be predicted to be either ablated away or in a heat-affected zone.

4.2. Parametric Study Results

4.2.1. Water addition and ingression

The base case CORQUENCH results assumed the containment was flooded at 15 h after SCRAM. It was also assumed that water addition was high enough to keep the debris covered with water. To bound the analyses, the case of no water addition was simulated.

As expected, with no water addition, the melt was predicted not to solidify within the 2 days of simulation time in CORQUENCH (Table VIII). There was considerable ablation in the sump region as well as the other regions. However, the concrete ablation rates in all of the regions, except the sump, were quite low or zero at the end of the simulation. In the sump region, the ablation rate had slowed to 7.2 mm/h by the end of the simulation.

Table VIII. Impact of water injection on core melt progression

Case	Long-term containment condition	In sump region			Total H_2 gas released (kmoles)
		Time to solidification (min)	Axial ablation (cm)	Radial ablation (cm)	
MELCOR-1-A	**wet**	151	13.4	19.9	37.4
MELCOR-1-B	**dry**	>2880[a]	>81.4[a]	>96.3[a]	>613[a]
MAAP-HP-3-A	**wet**	1362	64.1	64.1	348
MAAP-HP-3-B	**dry**	>2880[a]	>87.9[a]	>87.9[a]	>348[a]
MAAP-LP-4-A	**wet**	1176	58.8	58.8	345
MAAP-LP-4-B	**dry**	>2880[a]	>86.6[a]	>86.6[a]	>350[a]

[a] Case did not fully solidify within 48 h of simulated time.

For cases in which the cavity was flooded, the deep melt pool in the sump was predicted to quench primarily as a result of water ingression into the top crust. Without water ingress, a conduction-limited crust would form on top of the melt. For the current MCCI scenarios with melt decay heats in the range of 106–125 W/kg UO_2, the conduction-limited crust thickness was in the range of 15.0–16.3 cm. Codes such as CORCON-Mod3 (in MELCOR) that do not model the water ingression phenomenon cannot quench deep melt pools without modifying the melt properties, e.g. increasing the thermal conductivity by an order of magnitude. Although they are not included in the parametric study, simulations performed with an impervious crust would be bound by the wet and dry cases.

4.2.2. Containment pressure

The Unit 1 containment pressure varied between 0.84 and 0.74 MPa absolute from 12–22 h after SCRAM [1]. In the long term, 168–270 h after SCRAM, the pressure decreased to 0.17 MPa absolute [1]. The

containment pressure impacts the water saturation temperature, melt gas sparging rate due to core–concrete interaction, the volume flow rate of the sparged gas which influences phase stratification, and the top crust dry-out limit due to water ingression. In terms of the debris coolability models, increasing pressure reduces the potential for, and intensity of, the melt eruption cooling mechanism [16]; and the effectiveness of the water ingression cooling mechanism increases with increasing pressure. According to the Lomperski–Farmer water ingression model [14], the crust dry-out limit scales roughly with containment pressure raised to the 5/13 power. Thus changes in containment pressure during the sequence will cause the relative contributions of these two cooling mechanisms to fluctuate in opposing directions.

CORQUENCH uses a constant, user-specified containment pressure throughout the duration of a simulation. Cases were simulated in which the containment pressure was set to 0.35 MPa for comparison against the base case value of 0.75 MPa. A reduction in containment pressure slightly decreased the melt coolability, delaying the time to melt solidification, and increased the total amount of concrete ablation. However, the debris was still predicted to be coolable.

4.2.3. Melt-concrete crust formation and concrete ablation modeling

CORQUENCH contains three concrete ablation models [10]. The first (Model 1) is a quasi-steady ablation model in which all the heat transferred to the concrete is applied toward decomposing the concrete. This model is the same as that employed in CORCON-Mod3 (MELCOR). The second model tracks the thermal boundary layer in the concrete, liberating water and other concrete decomposition products in the concrete as the thermal boundary layer passes through. In this model, the thermal boundary layer is initialized as fully developed. The third model (Model 3), used in the base case simulations, tracks the transient development of the thermal boundary layer in the concrete. The third model also models crust formation at the melt–concrete interface.

Table IX. Impact of interstitial crust formation and ablation model on core melt progression

Case	Crust and ablation model	In sump region			Total H_2 gas released (kmoles)
		Time to solidification (min)	Axial ablation (cm)	Radial ablation (cm)	
MELCOR-1-A	**Model 3**	151	13.4	19.9	37.4
MELCOR-1-D	**Model 1**	131	28.9	28.5	141
MAAP-HP-3-A	**Model 3**	13,62	64.1	64.1	348
MAAP-HP-3-D	**Model 1**	1,388	75.0	75.0	293
MAAP-LP-4-A	**Model 3**	1,176	58.8	58.8	345
MAAP-LP-4-D	**Model 1**	1,206	69.5	69.5	271

Table IX compares the melt progression results in the sump region for the quasi-steady ablation model (Model 1) and the transient model with interstitial crust formation (Model 3). The high initial melt temperature of the MAAP cases prevented the formation of interstitial crusts. Therefore, the difference between the MAAP cases is due to the difference in the ablation model. Only the gases in ablated concrete were released using Model 1, which resulted in less oxidation of the melt and less flammable gas generation. The relatively cool melt of the MELCOR case resulted in the formation of interstitial crusts when Model 3 was used. These interstitial crusts acted to insulate the concrete early in the transient. Eventually, the interstitial crust re-melted and concrete ablation progressed uninhibited. The combined effect of the interstitial crusts and transient ablation model resulted in much less ablation during the early

portion of the melt cooling transient for the MELCOR case. Melt progression predictions with tools that use a quasi-steady ablation model (e.g., CORCON-Mod3), and cannot predict the formation of interstitial crusts, will predict greater concrete ablation than tools that capture the transient process.

4.2.4. Decay heat level

The decay heat in the melt may be reduced by the volatilization of the radionuclides. To investigate the impact of reduced decay heat, the melt decay heat was reduced by 25%. As is to be expected, the decrease in decay heat increased the melt coolability (Table IX). For the MAAP cases, in which no interstitial crust formed and there was a long core–concrete interaction, the 25% reduction in decay heat resulted in approximately a 15% reduction in concrete ablation in the sump region. For the MELCOR case, in which an interstitial crust formed and the melt solidified in a couple of hours, the reduction in decay heat had a minor impact on the melt cooling and concrete ablation in the sump region.

Table X. Impact of decay heat level on core melt progression

Case	Decay heat (%)	In sump region			Total H_2 gas released (kmoles)
		Time to solidification (min)	Axial ablation (cm)	Radial ablation (cm)	
MELCOR-1-A	**100**	151	13.4	19.9	37.4
MELCOR-1-E	**75**	151	13.5	13.6	32.9
MAAP-HP-3-A	**100**	1362	64.1	64.1	348
MAAP-HP-3-E	**75**	1121	53.9	53.9	345
MAAP-LP-4-A	**100**	1176	58.8	58.8	345
MAAP-LP-4-E	**75**	957	49.9	49.9	342

4.2.5. Crust anchoring to concrete surfaces

Crust anchoring to the concrete sidewalls and subsequent separation of the crust from the melt pool was disabled for the base case (1) model setup. Because of the scale of the tests, crust anchoring has occurred in a majority of past laboratory-scale MCCI tests [10]. Crust anchoring was observed in the largest MCCI test, MACE-M3b, that was 1.2×1.2 m, used LCS type concrete, did not have ablatable walls, and lacked heating in the solidified material [17]. However, during the test, approximately one third of the anchored crust failed and relocated downward. It is unclear whether crust anchoring would occur in the 1.45 ×1.45 m sumps in 1F1. To investigate the possibility of crust anchoring, simulations were conducted with the crust anchoring model enabled.

Crust anchoring was predicted to occur in the sumps for every case, and continued concrete ablation after 2 days of simulation time (Table XI). Only the MELCOR case was predicted to anchor in the edge pedestal region. The larger initial melt depth for this case allowed for a crust to develop that was thick enough to support itself. Finally, crust anchoring was predicted to occur in the doorway. Like the sumps, this region consisted of a small area confined by walls. However, there were only two walls; the other "walls" were debris in the neighboring regions. The unique boundary conditions of this region were captured only in basic detail. It is currently thought that crust anchoring and separation of the melt pool from the crust are unlikely at the pedestal scale. However, there is a possibility of crust anchoring in the sumps.

Table XI. Impact of crust anchoring on core melt progression

Case	Crust anchoring enabled	In sump region			Total H_2 gas released (kmoles)
		Time to solidification (min)	Axial ablation (cm)	Radial ablation (cm)	
MELCOR-1-A	**no**	151	13.4	19.9	37.4
MELCOR-1-F	**yes**	2880[a]	51.2[a]	65.6[a]	305[a]
MAAP-HP-3-A	**no**	1362	64.1	64.1	348
MAAP-HP-3-F	**yes**	2880[a]	86.8[a]	86.8[a]	348[a]
MAAP-LP-4-A	**no**	1176	58.8	58.8	345
MAAP-LP-4-F	**yes**	2880[a]	85.1[a]	85.1[a]	347[a]

[a] Case did not fully solidify within 48 h of simulated time.

5. CONCLUSIONS

The base case results of the long-term debris coolability analysis with CORQUENCH assumed sufficient water was injected into the containment to cover the debris, starting 15 h after shutdown. Under this condition, the simulations indicate that the melt was coolable over the long term. The predicted concrete ablation was less than the extent necessary to reach the liner through downward melt progression. The MELCOR case, which contained relatively cool melt, readily cooled within 2.5 h after relocation with limited concrete ablation in the sump regions (~18 cm) and less than 10 cm ablation elsewhere. Seventy-six kg of hydrogen and 103 kg of carbon monoxide were predicted to be generated during core–concrete interactions. The MAAP cases, which contained relatively hot melt, cooled approximately 22.5 h after melt relocation and resulted in 65 cm of concrete ablation in the sump region and less than 23 cm elsewhere in the containment. Large amounts of hydrogen (700 kg), carbon monoxide (750 kg), and carbon dioxide (490 kg) were predicted to be generated during concrete ablation for the MAAP cases.

The CORQUENCH calculations predicted that even though very deep melt pools may have formed during the 1F1 accident as a result of very high predicted core release fractions [1, 2], the debris is coolable. This is primarily due to two factors. First, the decay heat was relatively low several hours after SCRAM. Most of the MCCI experiments to date have simulated decay heat levels that are representative of 2 hours of decay time after SCRAM. The decay heat level in the current simulations was approximately 1/3 that of the previous experimental and analysis focus. Second, the debris dry-out heat flux, as predicted by the Lomperski-Farmer model [14], was augmented by the high containment pressure (scales to the 5/13 power with containment pressure). However, the dry-out limit was reduced by the addition of concrete oxides. For the MELCOR cases, there was very limited concrete ablation and the dry-out limit remained high. For the MAAP cases, there was concrete ablation, with considerable ablation occurring in the sump region, resulting in a reduced dry-out limit. However, as the concrete was laterally ablated in the sumps, the cross sectional area in contact with the overlying water increased. For both the MELCOR and MAAP cases, the net effect of these factors resulted in dry-out limits that were high enough to remove the decay heat even for the deep melt pools in the sump region. Note that the water ingression model was adapted from a theory developed for the field of volcanology; it has been successfully compared with field data for the cooling of several meters of lava [21] and is supported by the results of the reactor-material SSWICS test series [22].

ACKNOWLEDGMENTS

This work was supported by the US Department of Energy Office of Nuclear Energy. This support is greatly appreciated.

REFERENCES

1. R. O. Gauntt, et al., *Fukushima Daiichi Accident Stud*y, SAND2012-6173, Sandia National Laboratories (July 2012).
2. D. Luxat and J. Gabor, *Fukushima Technical Evaluation: Phase 1—MAAP5 Analysis*, Electric Power Research Institute, 1025750 (2013).
3. Nuclear Emergency Response Headquarters, Government of Japan, *Report of Japanese Government to the IAEA Ministerial Conference on Nuclear Safety—The Accident at TEPCO's Fukushima Nuclear Power Stations* (June 2011).
4. Y. Yamanaka, "Research Plan Regarding Improvement of Simulation Code for Understanding the Status of Fuel Debris in the Reactor," *International Symposium on the Decommissioning of TEPCO's Fukushima Daiichi Nuclear Power Plant Unit 1-4*, Tokyo, Japan, March 14, 2012 (2012).
5. Tokyo Electric Power Company, Inc., "Amendments to the Estimate Value of the Core Damage Ratio of Unit 1 to 3 of Fukushima Daiichi Nuclear Power Station based on the Measurement of the Containment Atmospheric Monitoring System," press release (April 27, 2011).
6. Tokyo Electric Power Company, Inc., "The Evaluation Status of Reactor Core Damage at Fukushima Daiichi Nuclear Power Station Units 1 to 3," press release handout (November 30, 2011).
7. Tokyo Electric Power Company, Inc., "Various Approaches for Understanding State of Nuclear Fuel," press release handout (November 30, 2011).
8. M. T. Farmer, J. J. Sienicki, and B. W. Spencer, "The MELTSPREAD-1 Computer Code for the Analysis of Transient Spreading in Containments," *Proc. of ANS Winter Meeting*, Washington D.C., November 11–15, 1990 (1990).
9. M. T. Farmer, J. J. Sienicki, C. C. Chu and B. W. Spencer, *The MELTSPREAD 1 Code for Analysis of Transient Spreading and Cooling of High-Temperature Melts, Code Manual*, EPRI TR-103413 (1993).
10. M. T. Farmer, *The CORQUENCH Code for Modeling of Ex–vessel Corium Coolability Under Top Flooding Conditions, Code Manual – Version 3.03*, OECD/MCCI-2010-TR03, Organisation for Economic Co-operation and Development (2010).
11. M. T. Farmer, "Modeling of Ex–vessel Corium Coolability with the CORQUENCH Code," *Proc. of ICONE-9*, Nice, France (2001).
12. K. R. Robb, M. W. Francis, and M. T. Farmer, E*nhanced Ex–vessel Analysis for Fukushima Daiichi Unit 1: Melt Spreading and Core-Concrete Interaction Analyses with MELTSPREAD and CORQUENCH*, ORNL/TM-2012/455, Oak Ridge National Laboratory (2013).
13. M. T. Farmer, K. R. Robb, and M. W. Francis, "Fukushima Daiichi Unit 1 Ex–vessel Prediction: Core Melt Spreading," *Proc. of NURETH-16*, Chicago, August 30–September 4, 2015 (2015).
14. S. Lomperski and M. T. Farmer, "Experimental Evaluation of the Water Ingression Mechanism for Corium Cooling," *Nucl. Eng. Design*, **237**, p. 905 (2006).
15. Japan Atomic Energy Agency, "Radioactivity analysis of reactor building core boring sample," August 29, 2013, http://www.meti.go.jp/earthquake/nuclear/pdf/130828/130828_01nn.pdf, in Japanese.
16. M. T. Farmer, "Phenomenological Modeling of the Melt Eruption Cooling Mechanism During Molten Corium Concrete Interaction (MCCI)," *Proceedings ICAPP '06*, Reno, Nevada, June 6–8, 2006 (2006).
17. M. T. Farmer, R. W. Aeschlimann, D. J. Kilsdonk, and B. W. Spencer, Results of MACE Test M3b Posttest Debris Characterization, EPRI/ACEX-TR-C32, Electric Power Research Institute (2000).
18. M. Cranga, et al, "Towards an European consensus on possible causes of MCCI ablation anisotropy in an oxidic pool," *Proc. of ERMSAR-2013*, Avignon, FR, October 2-4, 2013.
19. K. M. Kang, M. L. Corradini, "Phenomenological Modeling Approach to Anisotropic Ablation in Molten Core Concrete Interactions," *Proc. of NURETH-16*, Chicago, August 30–September 4, 2015 (2015).
20. L.T. Phan, *Fire Performance of High-Strength Concrete: A Report of the State-of-the-Art*, NISTIR 5934, National Institute of Standards and Technology (December 1996).
21. M. Epstein, "Dryout Heat Flux During Penetration of Water Into Solidifying Rock," *J. Heat Transfer* **128**, p. 847 (2006).
22. S. Lomperski and M. T. Farmer, "Experimental Evaluation of the Water Ingression Mechanism for Corium Cooling," *Nucl. Eng. Design* **237**, p. 905 (2006).